nature photonics

Article

https://doi.org/10.1038/s41566-026-02028-5

High-entropy molecular contacts enable high-efficiency and stable perovskite solar cells

Received: 21 April 2026

Accepted: 14 September 2026

Published online: 09 October 2026

Check for updates

Deng Wang[1,2,7], Mingqian Chen[1,2,7], Jiacong Feng[3,7], Qian Li[1,2,4], Chun-To Wong[1,4], Guanghui Lei[3], Qing Jiang[3], Tonghui Wang[3] ✉, Wenlin Jiang[1,5] ✉ & Alex K.-Y. Jen[1,2,4,6] ✉

The performance of inverted perovskite solar cells critically depends on the molecular contact formed by hole-selective self-assembled molecules. Conventional single-component hole-selective self-assembled molecules are prone to structural collapse under external stress, which disrupts hole transport and accelerates device degradation. Here we develop high-entropy molecular contacts (HE-MCs) by using a ternary blend of carbazole-naphthalene self-assembled molecules to simultaneously enhance device efficiency and operational stability. By blending molecules with similar chemical structures but distinct intermolecular interactions and packing motifs, we increase the packing-mode diversity to form a high-entropy system that affords efficient hole extraction and robust interfaces. Single-crystal analysis, molecular dynamics simulations and interfacial characterizations collectively confirm the successful formation of HE-MCs and their substantially improved resilience to external stress. Perovskite solar cells incorporating HE-MCs achieve a champion power conversion efficiency of 27.50% (certified steady-state efficiency of 27.31%) and extended operational stability under various accelerated ageing tests, with negligible efficiency loss after 1,300 h under maximum power point tracking at 85 °C in ambient air. Our strategy provides a broadly applicable framework that exploits high entropy in packing modes for high-performance interfaces in perovskite photovoltaic devices.

Molecular contacts (MCs) based on hole-selective self-assembled molecules (HSMs) have recently boosted the power conversion efficiency (PCE) of single-junction perovskite solar cells (PSCs) to 28.0%[1–4], spurring continuous performance breakthroughs in both varied-bandgap PSCs and tandem devices. Despite these advances, a widespread concern regarding the long-term stability of devices arises from the collapse of ordered packing of single-component HSMs[5–9]. Such collapse disrupts hole transport and accelerates device degradation, necessitating robust HSM contact strategies[10–12].

Compared with single-component systems, high-entropy materials formed from blending rationally designed multicomponent systems exhibit remarkable properties across diverse materials[13–15]. In high-entropy alloys and oxides, entropy gain confers phase stability, tunable kinetics and superior mechanical properties[16], typically arising from configurational disorder in inorganic mixtures or structural diversity in organic non-conjugated small molecules[17–19]. Nevertheless, developing high-entropy packing in HSM systems—dominated by strong π–π and hydrogen-bonding interactions—to prevent MC collapse

A full list of affiliations appears at the end of the paper. ✉e-mail: twang@jlu.edu.cn; jiangwlin@mail.sysu.edu.cn; alexjen@cityu.edu.hk

https://doi.org/10.1038/s41566-026-02028-5

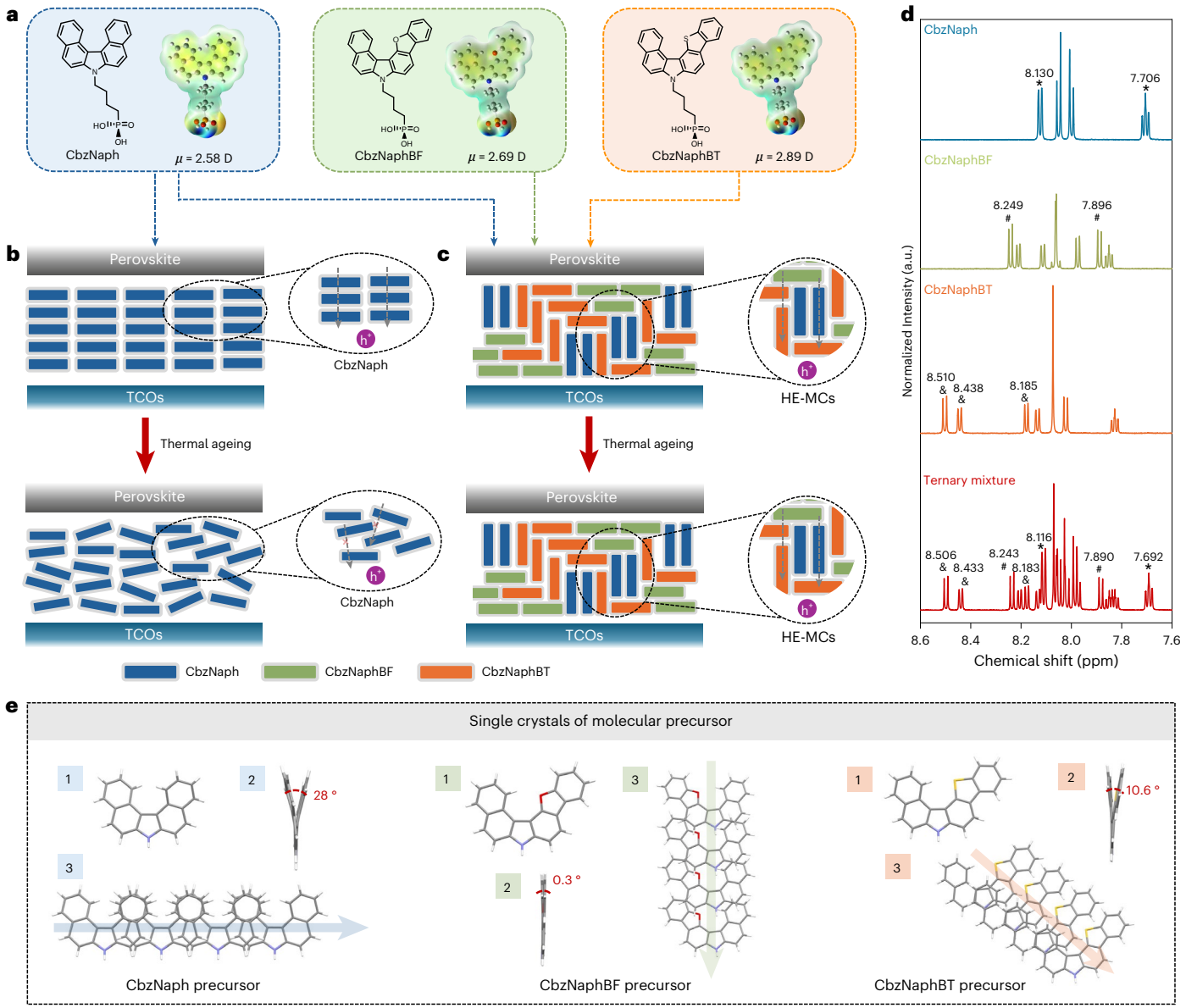


Fig. 1 | Molecular design rule for HE-MCs and intrinsic properties. a, The molecular structure and electrostatic potential surfaces of CbzNaph, CbzNaphBF and CbzNaphBT. **b**,**c**, Schematics of the evolution in molecular stacking and carrier transport pathways in CbzNaph (**b**) and HE-MC (**c**) films under thermal stress. **d**, Comparisons of ^{1}H NMR spectra of single-component molecules and their ternary mixture. The *, # and & symbols denote the characteristic peaks of CbzNaph, CbzNaphBF and CbzNaphBT in ^{1}H NMR spectra, respectively. **e**, Molecular packing patterns in single crystals corresponding to the molecular precursors of CbzNaph, CbzNaphBF and CbzNaphBT.

remains unexplored[20,21]. The key challenge is balancing ordered HSM self-assembly with high-entropy structural complexity while maintaining efficient hole transport.

Here, we report a strategy to construct high-entropy MCs (HE-MCs) at the hole-selective interface by blending several rationally designed HSMs with similar chemical structures but non-centrosymmetric units, which facilitate intricate stacking. Upon mixing, these molecules increase configurational disorder and successfully form HE-MCs. Molecular dynamics (MD) simulations, structural analysis and charge-transfer dynamics confirm that HE-MCs possess diverse and stable packing modes while maintaining efficient charge transport and extraction channels under thermal ageing. Consequently, the champion inverted PSC based on the HE-MCs achieves a certified steady-state PCE of 27.31%. The encapsulated device shows negligible decay of its initial PCE after maximum-power-point (MPP) tracking at 85 °C for 1,300 h under continuous one-sun illumination (ISOS-L-2 protocol).

Molecular design rule and intrinsic properties

The assembly of HSMs is typically governed by the interplay of multiple non-covalent interactions, such as π–π stacking, hydrogen bonding and C–H···π interactions[22–24]. For constructing HE-MCs, we propose to incorporate HSMs with similar chemical backbones while introducing additional distinct intermolecular interactions through targeted molecular modifications. This approach effectively generates diverse interactive motifs within the multicomponent system to increase configurational entropy.

CbzNaph has significantly improved efficiency in various PSCs owing to its helical backbone that enhances π–π interactions, dipole moments and solubility, favouring ordered MC formation[25,26]. However, this order renders CbzNaph susceptible to stress-induced collapse. To address this, we modified the conjugated framework of CbzNaph, preserving the helical benefits while disrupting symmetry and introducing heteroatoms to tune packing. Specifically, replacing

https://doi.org/10.1038/s41566-026-02028-5

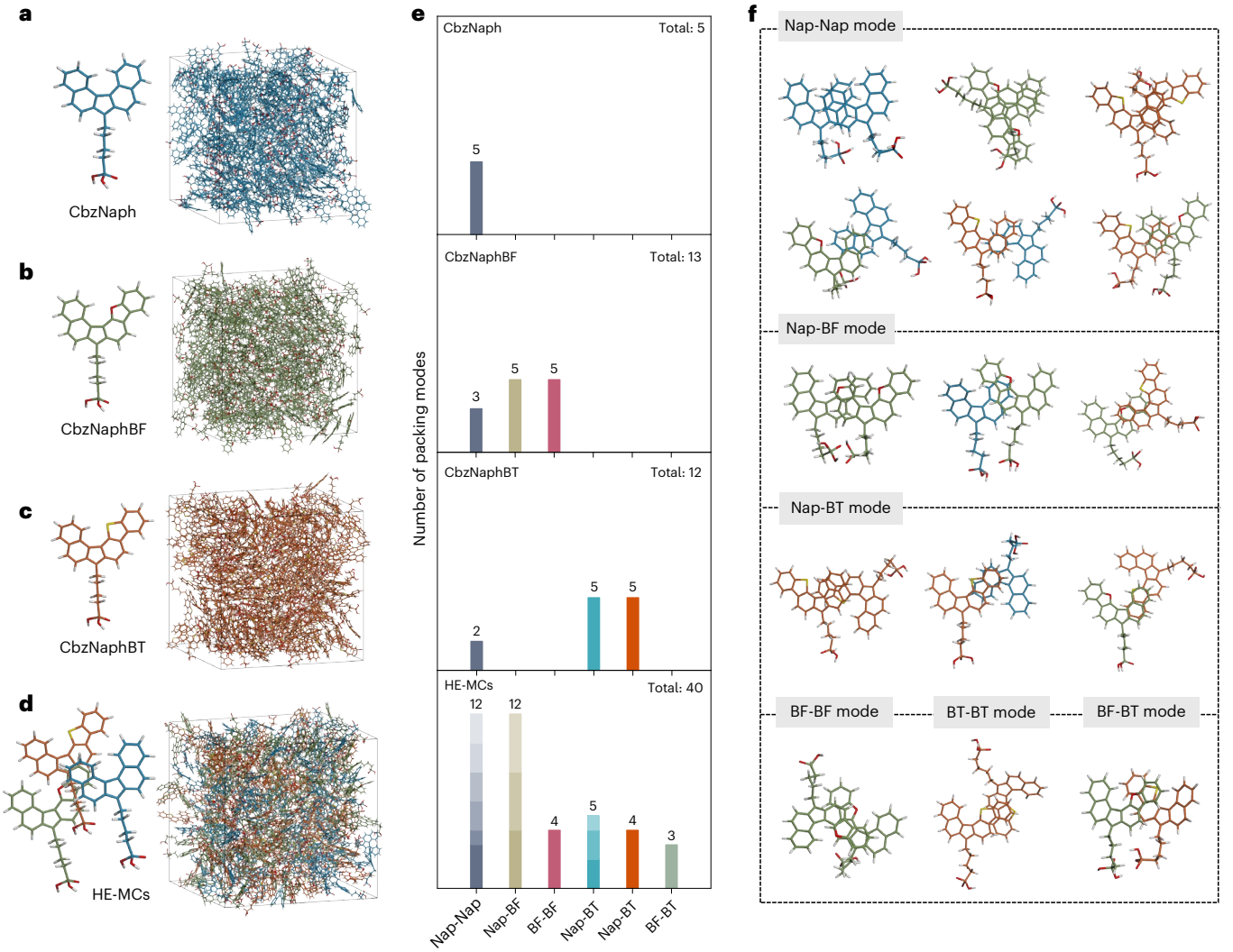


Fig. 2 | MD simulations. a–**d**, MD simulation models of the CbzNaph (**a**), CbzNaphBF (**b**) and CbzNaphBT (**c**) single-component systems, and the ternary-mixed HE-MC system (**d**). **e**, The summaries of packing models extracted from three single-component systems and HE-MC system; the gradient colours also represent the subdivision of packing for homo-molecular and hetero-molecular interactions. **f**, The specific packing modes extracted from the HE-MC system, including both homo-molecular and hetero-molecular interactions.

one naphthalene unit with dibenzofuran or dibenzothiophene yielded CbzNaphBF and CbzNaphBT, respectively (Fig. 1a). Their synthesis, confirmed by $^{1}H/^{13}C$ NMR and high-resolution mass spectrometry, is detailed in Supplementary Note 1 and Supplementary Figs. 1–22. All three HSMs showed comparable optical bandgaps and decomposition temperatures (Supplementary Fig. 23 and 24). Cyclic voltammetry yields highest occupied molecular orbital (HOMO) levels of −5.36, −5.42 and −5.43 eV for CbzNaph, CbzNaphBF and CbzNaphBT, respectively (Supplementary Note 2 and Supplementary Fig. 25), consistent with density functional theory (DFT) calculations[27] (Supplementary Fig. 26). Furthermore, the DFT-calculated molecular dipole moments increased from 2.58 Debye for CbzNaph to 2.69 and 2.89 Debye for CbzNaphBF and CbzNaphBT (Supplementary Fig. 27), respectively, demonstrating the enhanced tunability of work functions of transparent conductive oxides.

The ternary blend system is accordingly designed to increase the variety of molecular packing modes without compromising the efficient hole-transport channels of the resulting HE-MCs. Systematic optimization confirmed that the optimal ternary blend consists of a 1:1:1 equimolar ratio of CbzNaph, CbzNaphBF and CbzNaphBT (Supplementary Note 3 and Supplementary Figs. 28–30). The highly dispersed, intertwined molecular arrangement in HE-MCs not only endows them with superior resistance to structural degradation but also preserves efficient hole-transport channels, outperforming the single-component CbzNaph-derived MC (Fig. 1b,c). The ^{1}H NMR spectrum of the ternary mixture shows peak shifts relative to single-component spectra (Fig. 1d and Supplementary Table 1), indicating substantial intermolecular interactions among the three components and suggesting similar interactions may persist in thin films to facilitate HE-MC formation. The concentration-dependent UV–visible absorption spectra reveal a new broad peak (Supplementary Fig. 31), indicating strong interactions among the three molecules. Similar spectral changes in binary blends further confirm that blending chemically similar derivatives fosters close contacts (Supplementary Fig. 32), beneficial for constructing HE-MCs with varied interaction motifs. Moreover, these diverse interactions suppress the aggregation tendency observed in single-component solutions, effectively preventing the formation of large micelles during dissolution and dispersion, as confirmed by dynamic light scattering (Supplementary Fig. 33).

To verify the effects of asymmetric conjugation and heteroatoms on intermolecular interactions, we resolved the single-crystal structures of CbzNaphBF and CbzNaphBT precursors[25,27] (Fig. 1e and

https://doi.org/10.1038/s41566-026-02028-5

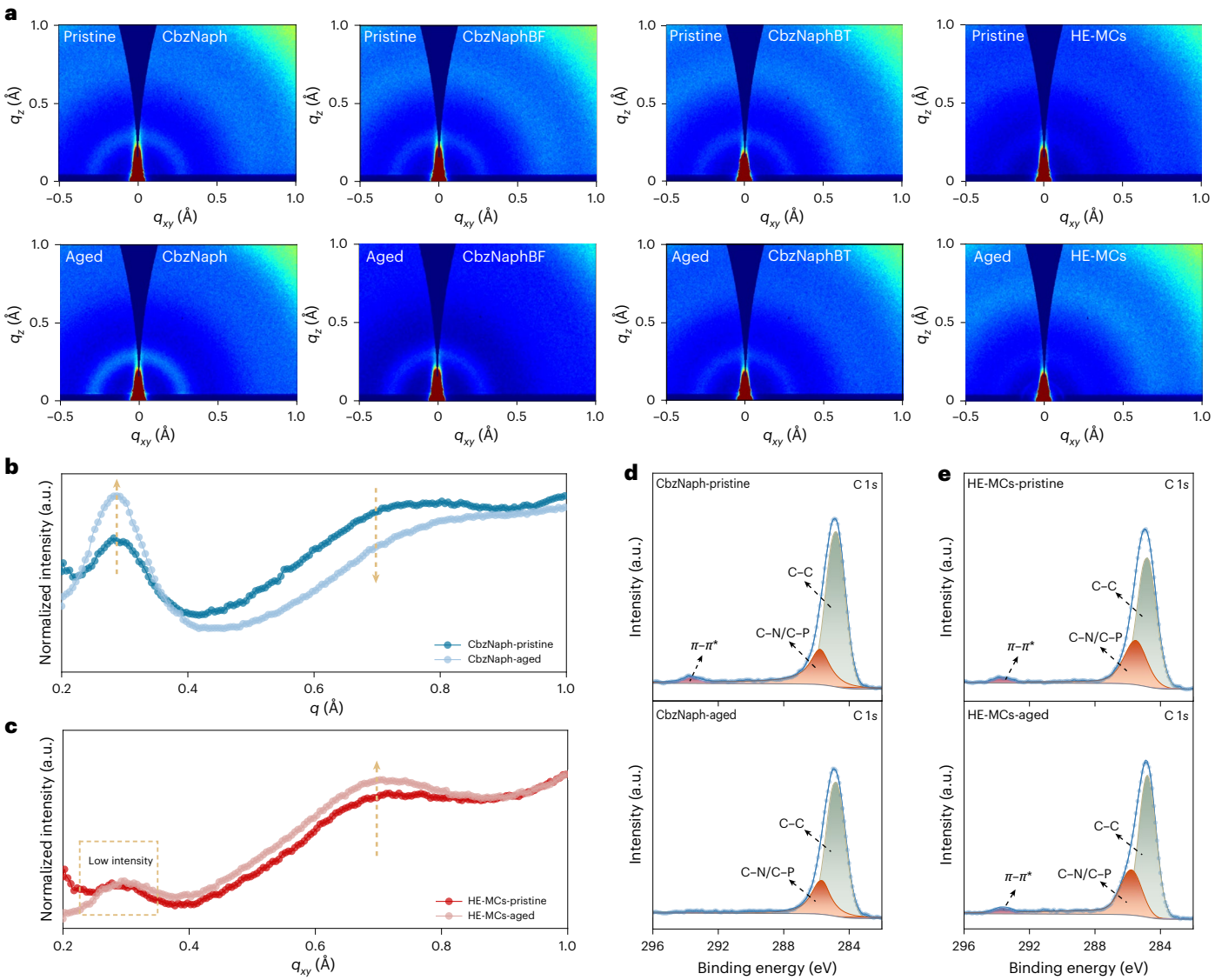


Fig. 3 | Structural and stacking properties of molecular films. a, GIWAXS patterns of pristine and aged HSM films drop-coated on silicon wafers converted to *q*-space. **b**,**c**, One-dimensional intensity profiles of the corresponding GIWAXS patterns for CbzNaph (**b**) and HE-MCs (**c**). **d**,**e**, High-resolution XPS spectra of C 1*s* for CbzNaph (**d**) and HE-MCs (**e**) deposited on FTO.

Supplementary Figs. 34–36). Compared with CbzNaph, the modified frameworks show reduced steric hindrance and torsional angles, with CbzNaphBF exhibiting the smallest helical angle of 0.3°, whereas CbzNaph and CbzNaphBT exhibit angles of 28° and 10.6°, respectively. In CbzNaph crystals, molecules form ordered one-dimensional π–π stacks in a herringbone pattern along the *a* axis, with additional C–H···π interactions between pillars. The increased planarity and C–H···O interactions in CbzNaphBF promote longitudinal slippage along the *b* axis, yielding a more ordered herringbone structure. By contrast, CbzNaphBT displays complex packing due to its helical skeleton, sulfur incorporation and asymmetric conjugation, with obliquely slipped stacks along the *a* axis via continuous C–H···π and C–H···S networks, resulting in two interpenetrating herringbone patterns in the chiral space group $P2_12_12_1$.

The single-crystal analysis confirms that our design controls packing orientations, with CbzNaphBT exhibiting a complex structure. Co-crystallization attempts yielded only twins or polycrystals, supporting a disordered high-entropy state upon mixing. Therefore, we conclude that a ternary-mixed system comprising CbzNaph, CbzNaphBF and CbzNaphBT can successfully form HE-MCs via distinct interactions and stacking modes.

Theoretical calculations for HE-MCs

We first built the geometry models of single-component HSMs assembled on the fluorine-doped tin oxide (FTO) surface and generated the corresponding charge-density difference maps for comparison (Supplementary Figs. 37 and 38). CbzNaphBT showed more pronounced electron redistribution than CbzNaph and CbzNaphBF under both anchoring configurations, creating a stronger internal electric field at the hole-selective interface for rapid hole transfer[28].

To investigate the dynamic self-assembling process during rapid MC deposition, we performed MD simulations to analyse the molecular packing modes. Three boxes of 200 pure molecules (CbzNaph, CbzNaphBF or CbzNaphBT) and one mixed box (1:1:1) were thermally annealed (Fig. 2a–d). After equilibrium at room temperature, the detailed packing patterns were extracted from the MD simulations and systematically analysed (Fig. 2e). CbzNaph formed only one packing pattern, primarily driven by interactions with the naphthalene moiety, which is defined as 'Nap-Nap'. By contrast, besides the packing modes of Nap-Nap, the non-centrosymmetric structures of CbzNaphBF and CbzNaphBT led to greater complexity in packing

https://doi.org/10.1038/s41566-026-02028-5

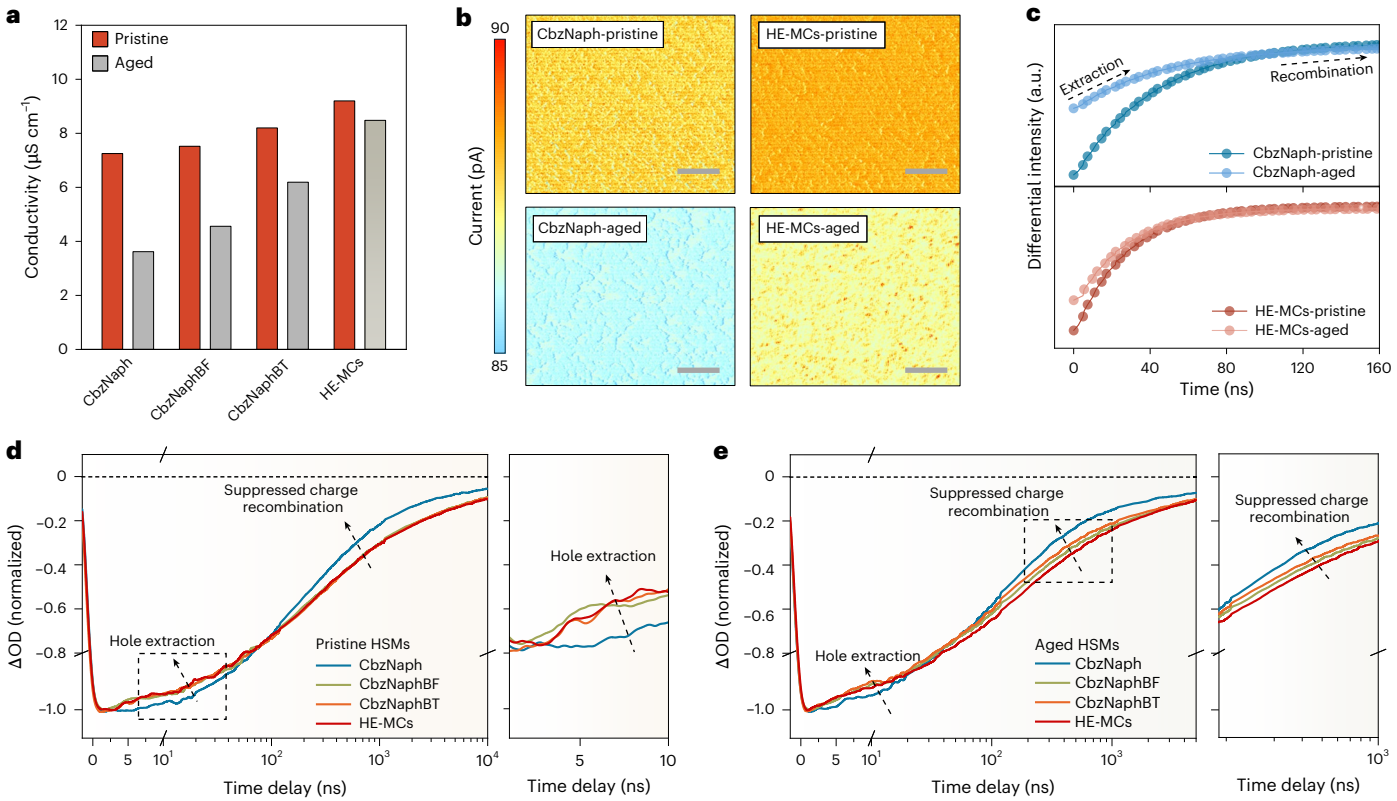


Fig. 4 | The evaluation of carrier behaviours. a, The measured conductivity of pristine and aged HSMs using hole-only device architecture. **b**, Conductive-AFM images and surface current signals of CbzNaph and HE-MCs films before and after ageing treatment (scale bar, 1 μm). **c**, The differential intensity of TRPL spectra for CbzNaph-based and HE-MC-based perovskite stacks before and after ageing treatment (the light was incident from FTO glasses). **d**,**e**, Nanosecond-TAS decay kinetics of perovskite stacks based on different HSMs before ageing treatment (**d**) and the corresponding kinetics after ageing treatment (**e**). ΔOD, change in optical density.

(both in three categories), including naphthalene-dibenzofuran/thiophene (Nap-BF/BT), dibenzofuran-dibenzofuran (BF-BF) and dibenzothiophene-dibenzothiophene (BT-BT). A comparative study of the binary systems revealed that the CbzNaphBF/CbzNaphBT system yields a total of 26 molecular packing modes, more than the 17 and 20 modes observed for the CbzNaph/CbzNaphBF and CbzNaph/CbzNaphBT systems (Supplementary Fig. 39), respectively, further confirming that the non-centrosymmetric structures of CbzNaphBF and CbzNaphBT enhance the packing complexity.

Notably, more complex molecular packing can be established in the HE-MC system. Alongside the homo-molecular interactions observed in the single-component systems, several novel hetero-molecular packing modes emerged (Fig. 2f and Supplementary Table 2), including Nap-Nap, Nap-BF, Nap-BT and BF-BT arrangements, yielding 15 categories of packing modes. Further analysis of the directions and angles of molecular dimer formation in the model reveals that a total of 40 molecular packing modes can be obtained from the HE-MC, far exceeding the value observed in the single-component system. A similar trend towards increased molecular packing diversity could also be observed in the HE-MCs assembled on FTO substrates (Supplementary Fig. 40) compared with that in the single-component molecular system. Therefore, both asymmetric design and ternary blending substantially increased the diversity of microscopic stacking modes. Through statistical analysis of the number fraction of each packing mode, the resulting mixing entropy $\triangle S_{mix}$ was determined to be 12.89 J mol^{-1} K^{-1} following Flory–Huggins theory[29] (Supplementary Note 4 and Supplementary Table 3), which corresponds to 1.55 R, confirming the formation of a high-entropy configurational structure in the ternary MC system.

Diversifying the stacking modes in HE-MC films not only increases macroscopic entropy but also preserves short-range ordered stacks through specific interactions, which are essential for efficient hole transport. To verify this, we performed a weighted statistical analysis of hole-transport rates on the basis of molecular packing patterns and component ratios in both single-component and ternary systems (Supplementary Table 4). The calculated average hole-transport rates for CbzNaph, CbzNaphBF and CbzNaphBT were 1.81×10^{13} s^{-1}, 2.02×10^{13} s^{-1} and 2.17×10^{13} s^{-1}, respectively. Remarkably, the average rate in the ternary HE-MC increased to 2.72×10^{13} s^{-1}, demonstrating the enhanced hole-extraction capability of the HE-MC system.

Structural and stacking properties of molecular films

The structural evolution of the HSM films under thermal stress was investigated using grazing-incidence wide-angle X-ray scattering (GIWAXS) (Fig. 3a). Note that HSM films were prepared by drop-coating from 10-mM solutions, and thermally aged at 85 °C for 100 h. These ageing conditions were used for other characterizations unless otherwise specified. For the pristine CbzNaph, CbzNaphBF and CbzNaphBT films, a distinct diffraction ring at $q = 0.3$ Å^{-1} was observed, and its intensity increased to varying degrees after thermal ageing, indicating enhanced long-range crystallinity and a tendency towards aggregation. To quantify this behaviour, we performed multi-peak fits of the one-dimensional GIWAXS profiles and extracted coherence lengths (CCLs) (Supplementary Table 5). The ageing-induced rise in fitted CCLs at $q = 0.3$ Å^{-1} across all three films indicates mesoscale ordering growth. CbzNaphBT, with only a weak corresponding ring, follows the same trend, reflecting the molecular structure-dependent nature of unidirectional long-range packing. By contrast, the HE-MC film exhibits only a weak low-q ring, reflecting a macroscopically disordered, multi-orientational packing that favours ensemble homogeneity.

https://doi.org/10.1038/s41566-026-02028-5

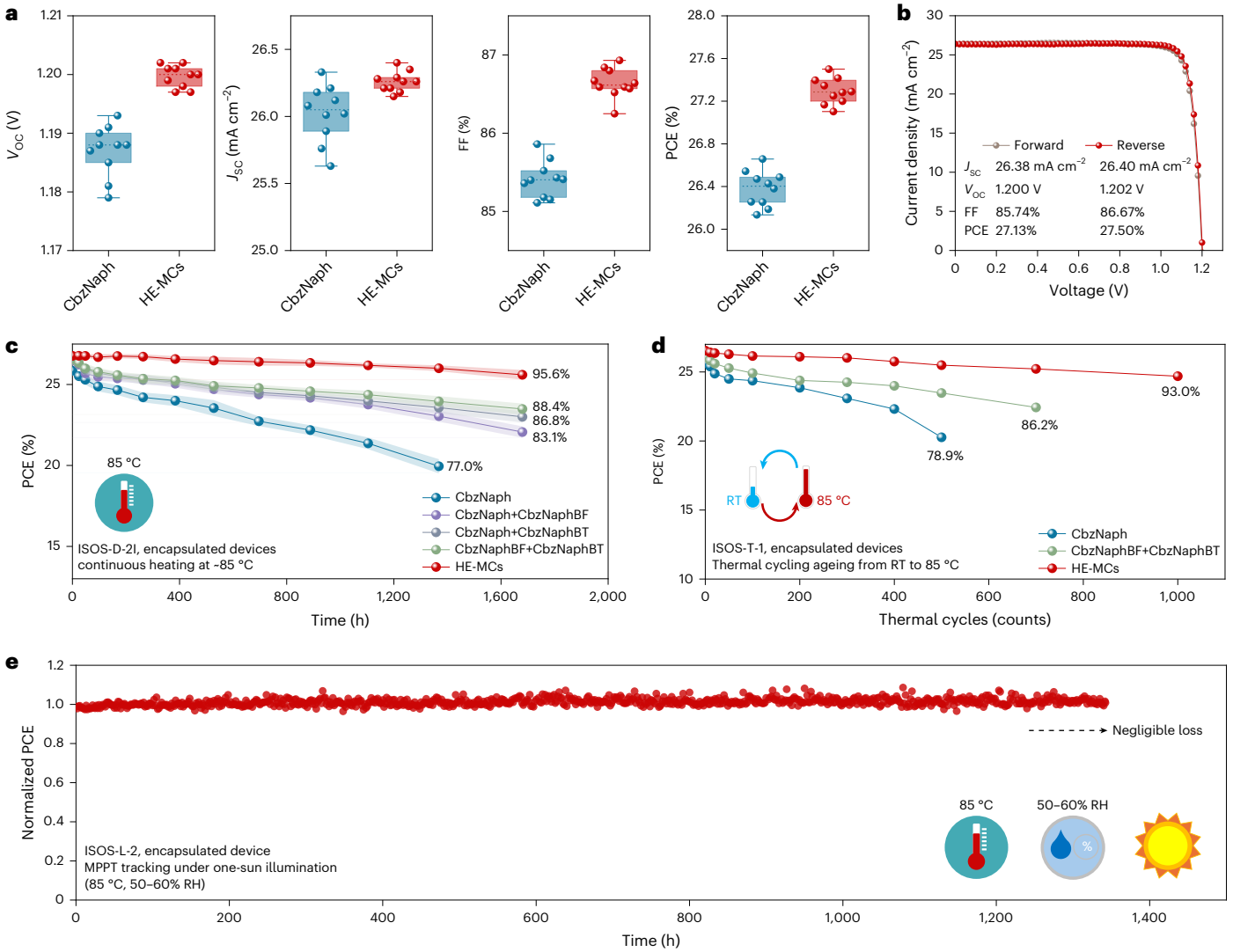


Fig. 5 | Photovoltaic performances and long-term stability. a, The statistics of the V_{OC}, J_{SC}, FF and PCE of devices based on CbzNaph and HE-MCs (ten devices of each type in a single batch). The upper and lower whiskers denote the maxima and minima; the box bounds correspond to the 25th and 75th percentiles; and the dashed centre line indicates the mean value. **b**, *J*–*V* curves of best-performing device based on HE-MCs from forward and reverse scan directions. **c**, Thermal stability of devices based on different HSMs heated at 85 °C in N_2 atmosphere following the ISOS-D-2I protocol. The PCE values presented as mean ± standard deviation (n = 3 individual devices per group). The error bars represent the standard deviation. **d**, Long-term stability of encapsulated devices under thermal cycling conditions (RT–85 °C) following the ISOS-T-1 protocol. **e**, Continuous MPP tracking of PCE for encapsulated devices heated at 85 °C in ambient air (50–60% relative humidity) following the ISOS-L-2 protocol. The initial PCE of the corresponding device was 25.02% when measured at RT. RT, room temperature; RH, relative humidity.

A detailed inspection of the integrated one-dimensional intensity at q = 0.7 Å^{-1} reveals that the relative intensity for CbzNaph (and similarly for CbzNaphBF and CbzNaphBT) decreases after ageing (Fig. 3b and Supplementary Fig. 41), indicating that short-range packing is more susceptible to thermal stress in single-component systems. By contrast, HE-MCs display a slight increase in intensity at q = 0.7 Å^{-1} after ageing (Fig. 3c), and its short-range coherence is preserved. This highlights how entropy-induced short-range order can stabilize the packing network against thermal stress, while avoiding the collapse often encountered in long-range-ordered single-component assemblies[30].

To further probe stacking evolution, we performed high-resolution X-ray photoelectron spectroscopy (XPS) measurements on HSM films (Supplementary Fig. 42). The C 1*s* spectra of the HSM films were mainly fitted by two distinguishable C–C and C–P/C–N carbon peaks. A π–π satellite peak at ~293.0 eV was observed in CbzNaph, CbzNaphBF and CbzNaphBT films (Fig. 3d and Supplementary Fig. 43), ascribed to ordered packing[31]. However, this π–π satellite disappeared after ageing, indicating thermal disruption of π–π interactions in single-component systems. By contrast, the HE-MC film retained the satellite under the same conditions (Fig. 3e), confirming that diverse packing modes sustain robust π–π interactions for efficient hole transport. We also performed nanoscale chemical imaging via atomic force microscopy-infrared spectroscopy (AFM-IR) measurements on the HE-MC films before and after thermal stress to directly visualize the spatial distribution of the HSM components (Supplementary Fig. 44). The AFM-IR images revealed that both CbzNaphBT and CbzNaphBF components were extensively and uniformly dispersed, resulting in a homogeneous HE-MC film. Remarkably, subjecting the film to thermal stress did not appreciably affect this distribution, and no phase separation phenomena were observed.

Evaluation of carrier behaviours

Hole-extraction capability under thermal stress was evaluated by conductivity measurements using the hole-only structure of

FTO/HSMs/MoO_3/Ag (ref. 32) (Supplementary Fig. 45, Supplementary Table 6 and Supplementary Note 5). The pristine HE-MCs showed the highest conductivity of 9.2 μS cm^{-1} among the tested HSMs, with minimal degradation upon ageing (Fig. 4a), indicating enhanced thermal resilience of HE-MCs. Conductive-AFM measurements further showed that HE-MC films exhibited superior charge transport despite lacking oriented stacking (Fig. 4b and Supplementary Fig. 46). Upon heating, the current signal of CbzNaph films dropped sharply, whereas HE-MC films maintained a high signal. The ultraviolet photoelectron spectroscopy measurements showed that HE-MCs exhibited improved energetic alignment at the hole-selective interface, reducing the hole-transfer barrier and suppressing interfacial recombination (Supplementary Figs. 47–49).

To systematically evaluate hole-transport behaviours from the perovskite sides, we fabricated the half-devices by depositing $Cs_{0.05}MA_{0.05}FA_{0.90}PbI_3$ perovskite films on HSM-modified substrates[33]. All HSMs exhibited good wettability for perovskite precursor deposition (Supplementary Fig. 50). The X-ray diffraction patterns and scanning electron microscopy images revealed similar crystallization orientations and surface morphologies for all perovskite films (Supplementary Figs. 51 and 52). To gain more insights into the impact of ageing conditions on charge carrier transfer, we measured the steady-state photoluminescence (PL) and time-resolved photoluminescence (TRPL) of perovskite stacks (Supplementary Figs. 53 and 54). The corresponding differential lifetime from TRPL measurements could also be derived using the formula $\tau = -[\mathrm{d}\ln(\mathrm{TRPL})/\mathrm{d}t]$, where t is the delay time. (ref. 34) (Fig. 4c and Supplementary Table 7). This analysis showed thermal ageing compromised the growth rate of differential intensity in CbzNaph, indicating retarded interfacial hole transfer. By contrast, the growth rate was preserved at a comparable level post-ageing in the HE-MCs cases, demonstrating their efficacy in preserving efficient hole transfer.

The benefits of as-designed HSMs on carrier dynamics were investigated by ultrafast transient absorption spectroscopy (TAS) measurements. The carrier transfer and recombination behaviours in different HSM/perovskite stacks were inferred from the ground-state bleaching (GSB) dynamics of perovskite. We conducted nanosecond-resolved TAS measurements by exciting the samples with a pump pulse at 650 nm, with all samples displaying prominent GSB peaks at around 790 nm (Supplementary Fig. 55 and Supplementary Note 6). The GSB signals in the stacks employing CbzNaphBF or CbzNaphBT decay faster than those from CbzNaph-based stacks in initial delay time, between 5 and 100 ns, which can be attributed to the enhanced hole extraction at the hole-selective interface (Fig. 4d). To exclude the degradation factors of perovskites under ageing conditions, we deposited the perovskite layers onto thermally aged HSMs for comparison. Notably, the HE-MC-based stacks exhibited nearly unchanged exciton dynamics and markedly suppressed charge recombination (Fig. 4e), as revealed by the GSB peaks in the delay time range of 100–1,000 ns, demonstrating the robust stacking stability of HE-MCs in maintaining carrier selectivity[35]. The XPS analysis of the buried perovskite interfaces peeled from different substrates revealed the enhanced coordination interactions of CbzNaphBF and CbzNaphBT with Pb^{2+} compared with CbzNaph (Supplementary Fig. 56), indicating the improved passivation effect on interfacial defects attributed to the introduction of heteroatoms.

Performance and stability of PSCs

To evaluate the HE-MC-based device performance, we fabricated inverted PSCs with the device configuration of FTO/HE-MCs/perovskite/fullerene (C_{60})/tin(IV) oxide (SnO_2)/Cu (Supplementary Fig. 57). Control devices based on single-component and binary-mixed HSMs were prepared in the same batch. The statistical device data are shown in Supplementary Figs. 58 and 59, and the corresponding photovoltaic parameters are summarized in Supplementary Table 8. The HE-MC-based devices showed improved average PCE from 26.37% to 27.29% compared with the CbzNaph-based device, accompanied by the enhanced open-circuit voltage (V_{OC}) and fill factor (FF) (Fig. 5a), which could be attributed to the enhanced hole-selectivity and interfacial passivation[36]. Among devices with different HSM systems (Fig. 5b and Supplementary Fig. 60), the champion cell yielded a PCE of 27.50% under reverse scan, with a V_{OC} of 1.202 V, a J_{SC} of 26.40 mA cm^{-2} and an FF of 86.67%, which also exhibited negligible hysteresis under forward scan. The integrated J_{SC} for the champion device generated from the external quantum efficiency (EQE) was determined to be 25.72 mA cm^{-2} (Supplementary Fig. 61), matching well with the J_{SC} obtained from J–V scan results. A fabricated cell was certified by the Tianjin Institute of Metrological Supervision and Testing to show a steady-state efficiency of 27.31% (Supplementary Fig. 62).

To probe the effect of HE-MCs on recombination behaviours, we analysed Nyquist plots from electrochemical impedance spectra (Supplementary Fig. 63). The HE-MC-based device has a much higher recombination resistance (R_{rec}) (1,375 Ω) than that of the CbzNaph-based device (825 Ω), indicating more efficient charge extraction and less recombination[37]. The charge-transfer dynamics in completed devices were further evaluated by transient photocurrent measurements (Supplementary Fig. 64). After ageing, the photocurrent decay time for CbzNaph-based devices increased from 1.61 to 7.32 μs, whereas for HE-MC devices it rose only from 1.41 to 2.19 μs, demonstrating superior resilience to thermal stress[38,39]. Leveraging the enhanced hole-selectivity of HE-MCs, we also fabricated 1.68-eV and 1.77-eV wide-bandgap PSCs, achieving open-circuit voltages of 1.283 V and 1.376 V, respectively, with both voltage losses below 0.4 V (Supplementary Figs. 65 and 66). For scalability, we fabricated twenty 1-cm^2 devices in one batch, which delivered a champion PCE of 25.92% and an average PCE of 25.32%, respectively (Supplementary Fig. 67), demonstrating good reproducibility of the HE-MC-based large-area devices.

We further evaluated the stability of HE-MC-based devices according to the International Summit on Organic Photovoltaic Stability (ISOS) protocols[40]. To systematically investigate the thermal stability, we also fabricated devices based on binary-mixed HSMs and periodically tested at 85 °C in N_2 following the ISOS-D-2I protocol (Fig. 5c). The CbzNaph-based devices exhibited abrupt PCE drops to below 80% of their initial values after 1,368 h, while the best-performing binary-HSMs-based device (CbzNaphBF/CbzNaphBT) and the HE-MC-based device retained ~88% and ~95% of their initial PCEs, respectively, after 1,680 h of ageing. The three devices were further subjected to thermal cycling ageing (room temperature to 85 °C) following the ISOS-T-1 protocol (Fig. 5d). The PCE of the CbzNaph-based device dropped to below 80% of its initial value after just 500 cycles, while that of binary-HSMs-based device fell to below 90% after 700 cycles. In stark contrast, the device incorporating HE-MC retained 93% of its initial PCE even after 1,000 cycles, confirming its superior resistance to thermal stress. Compared with the binary HSM counterpart, the enhanced stability of the device based on HE-MCs is attributed to both the evaluated conductivity of the HSM films and the corresponding hole-extraction process (Supplementary Figs. 68 and 69). Furthermore, the ISOS-L-2 protocol was conducted under MPP tracking with one-sun illumination at 85 °C in ambient air (Fig. 5e). The HE-MC-derived device exhibited exceptional stability, showing negligible efficiency loss after MPP tracking for 1,300 h. These comprehensive stability assessments highlight the potential of applying hole-selective HE-MCs for commercial photovoltaic applications.

Online content

Any methods, additional references, Nature Portfolio reporting summaries, source data, extended data, supplementary information, acknowledgements, peer review information; details of author contributions and competing interests; and statements of data and code availability are available at https://doi.org/10.1038/s41566-026-02028-5.

References

1. Jiang, W. et al. Toughened self-assembled monolayers for durable perovskite solar cells. *Nature* **646**, 95–101 (2025).
2. Li, M., Liu, M., Qi, F., Lin, F. R. & Jen, A. K. Self-assembled monolayers for interfacial engineering in solution-processed thin-film electronic devices: design, fabrication, and applications. *Chem. Rev.* **124**, 2138–2204 (2024).
3. Guo, J. et al. AI-guided design of efficient perovskite solar cells operationally stable at 100 °C. *Science* **392**, 724–728 (2026).
4. *Best Research-Cell Efficiency Chart* (National Laboratory of the Rockies, accessed 28 August 2026); https://www.nlr.gov/pv/cell-efficiency
5. Wang, X. et al. Regulating phase homogeneity by self-assembled molecules for enhanced efficiency and stability of inverted perovskite solar cells. *Nat. Photon.* **18**, 1269–1275 (2024).
6. Zhou, J. et al. Molecular contacts with an orthogonal π-skeleton induce amorphization to enhance perovskite solar cell performance. *Nat. Chem.* **17**, 564–570 (2025).
7. Tian, C. et al. Photostable donor–acceptor interface for minimizing energy loss in inverted perovskite solar cells. *Nat. Photon.* **20**, 287–295 (2026).
8. Yang, W. et al. Axially chiral molecular contacts with low isomerization barriers for perovskite solar cells. *Nat. Photon.* **20**, 232–240 (2026).
9. Fei, C. et al. Limiting phosphonic acid interlayer–perovskite reactivity to stabilize perovskite solar modules. *Science* **391**, eadz7969 (2026).
10. Dong, B. et al. Self-assembled bilayer for perovskite solar cells with improved tolerance against thermal stresses. *Nat. Energy* **10**, 342–353 (2025).
11. Luo, C. et al. Engineering bonding sites enables uniform and robust self-assembled monolayer for stable perovskite solar cells. *Nat. Mater.* **24**, 1265–1272 (2025).
12. Cho, Y. et al. Local phase-modulated heterostructures for perovskite solar cells with high-efficiency and ultra-stability. *Energy Environ. Sci.* **18**, 8161–8170 (2025).
13. Tian, Y. et al. High-entropy hybrid perovskites with disordered organic moieties for perovskite solar cells. *Nat. Photon.* **18**, 960–966 (2024).
14. Liu, X. et al. High-entropy lead-free organic-inorganic hybrid perovskites exhibiting broad absorption and bright golden emission for LEDs. *Angew. Chem. Int. Ed.* **138**, e16911 (2026).
15. Yao, Y. et al. High-entropy nanoparticles: synthesis–structure–property relationships and data-driven discovery. *Science* **376**, eabn3103 (2022).
16. Peng, Z., Ghasemi, M., Michels, J. J. & Ade, H. Re-entrant phase behaviour of organic semiconductors. *Nat. Mater.* **24**, 1785–1792 (2025).
17. Kim, G. et al. Ternary self-assembled molecular contact for ambient-processed perovskite/silicon tandem solar cells. *Nat. Photon.* **20**, 835–842 (2026).
18. Miao, T. et al. An entropy-regulating molecular lock stabilizes formamidinium lead halide perovskite. *Science* **392**, 742–748 (2026).
19. Kim, K. et al. Non-volatile solid-state 4-(*N*-carbazolyl)pyridine additive for perovskite solar cells with improved thermal and operational stability. *Nat. Energy* **10**, 1427–1438 (2025).
20. Gao, D. et al. High-efficiency perovskite solar cells enabled by suppressing intermolecular aggregation in hole-selective contacts. *Nat. Photon.* **19**, 1070–1077 (2025).
21. Wu, H. et al. Tailored lattice-matched carbazole self-assembled molecule for efficient and stable perovskite solar cells. *J. Am. Chem. Soc.* **147**, 8004–8011 (2025).
22. Guo, R. et al. Refining the substrate surface morphology for achieving efficient inverted perovskite solar cells. *Adv. Energy Mater.* **13**, 2302280 (2023).
23. Park, S. M. et al. Low-loss contacts on textured substrates for inverted perovskite solar cells. *Nature* **624**, 289–294 (2023).
24. Liu, S. et al. Buried interface molecular hybrid for inverted perovskite solar cells. *Nature* **632**, 536–542 (2024).
25. Jiang, W. et al. Expanded carbazoles as hole-selective self-assembled monolayers for high-performance perovskite solar cells. *Angew. Chem. Int. Ed.* **61**, e202213560 (2022).
26. He, R. et al. Improving interface quality for 1-cm^2 all-perovskite tandem solar cells. *Nature* **618**, 80–86 (2023).
27. Du, J. et al. Face-on oriented self-assembled molecules with enhanced π–π stacking for highly efficient inverted perovskite solar cells on rough FTO substrates. *Energy Environ. Sci.* **18**, 3196–3210 (2025).
28. Zeng, J. et al. Small-molecule hole transport materials for >26% efficient inverted perovskite solar cells. *J. Am. Chem. Soc.* **147**, 725–733 (2025).
29. Siber, M., Ronsin, O. J. J. & Harting, J. Extending the Flory–Huggins theory for crystalline multicomponent mixtures. *Macromolecules* **59**, 1953–1966 (2026).
30. Zhu, P. et al. Symmetry-driven engineering of long-range-ordered π–π stacking molecules for high-efficiency perovskite photovoltaics. *Nat. Synth.* **5**, 64–73 (2026).
31. Chen, M. et al. Crystal growth regulation of Ruddlesden–Popper perovskites via self-assembly of semiconductor spacers for efficient solar cells. *Angew. Chem. Int. Ed.* **136**, e202315943 (2024).
32. Li, C. et al. Fully aromatic self-assembled hole-selective layer toward efficient inverted wide-bandgap perovskite solar cells with ultraviolet resistance. *Angew. Chem. Int. Ed.* **63**, e202315281 (2024).
33. Zhu, P. et al. Aqueous synthesis of perovskite precursors for highly efficient perovskite solar cells. *Science* **383**, 524–531 (2024).
34. Peng, W. et al. A versatile energy-level-tunable hole-transport layer for multi-composition inverted perovskite solar cells. *Energy Environ. Sci.* **18**, 874–883 (2025).
35. Liu, K.-K. et al. Polymerized Y-series non-fullerene acceptors as robust electron-transporting layer for efficient inverted perovskite solar cells. *Joule* **9**, 101955 (2025).
36. Jiang, W., Hu, Y., Li, F., Lin, F. R. & Jen, A. K. Y. Hole-selective contact with molecularly tailorable reactivity for passivating high-performing inverted perovskite solar cells. *CCS Chem.* **6**, 1654–1661 (2024).
37. Zhang, X. et al. A spiro-type self-assembled hole transporting monolayer for highly efficient and stable inverted perovskite solar cells and modules. *Energy Environ. Sci.* **18**, 468–477 (2025).
38. Zhu, J. et al. A donor–acceptor-type hole-selective contact reducing non-radiative recombination losses in both subcells towards efficient all-perovskite tandems. *Nat. Energy* **8**, 714–724 (2023).
39. Park, J. et al. Stepwise volatilization induced by nature-sourced volatile solid additives improving the efficiency and stability of perovskite solar cells. *Energy Environ. Sci.* **18**, 6260–6272 (2025).
40. Khenkin, M. V. et al. Consensus statement for stability assessment and reporting for perovskite photovoltaics based on ISOS procedures. *Nat. Energy* **5**, 35–49 (2020).

Publisher's note Springer Nature remains neutral with regard to jurisdictional claims in published maps and institutional affiliations.

Springer Nature or its licensor (e.g. a society or other partner) holds exclusive rights to this article under a publishing agreement with the author(s) or other rightsholder(s); author self-archiving of the accepted manuscript version of this article is solely governed by the terms of such publishing agreement and applicable law.

© The Author(s), under exclusive licence to Springer Nature Limited 2026

[1]Department of Materials Science and Engineering, City University of Hong Kong, Kowloon, China. [2]Department of Chemistry, City University of Hong Kong, Kowloon, China. [3]Key Laboratory of Automobile Materials, Ministry of Education, School of Materials Science and Engineering, Jilin University, Changchun, China. [4]Hong Kong Institute for Clean Energy, City University of Hong Kong, Kowloon, China. [5]School of Chemical Engineering and Technology, Sun Yat-sen University, Zhuhai, China. [6]State Key Laboratory of Marine Environmental Health, City University of Hong Kong, Kowloon, China. [7]These authors contributed equally: Deng Wang, Mingqian Chen, Jiacong Feng. ✉e-mail: twang@jlu.edu.cn; jiangwlin@mail.sysu.edu.cn; alexjen@cityu.edu.hk

Methods

Materials

Lead(II) iodide (PbI_2, >99.0%) was purchased from TCI (Shanghai) Development. Caesium iodide (CsI, 99.9%), methylammonium iodide (MAI, 99.9%), formamidinium iodide (FAI, 99.9%), methylammonium chloride (MACl, 99.9%), ethanediamine dihydroiodide (EDADI, 99.5%), fullerene (C_{60}, 99.5%) and bathocuproine (BCP, 99.0%) were purchased from Xi'an Polymer Light Technology. 4-Guanidinobenzoic acid hydrochloride (GBAC, 99%) and piperazine hydroiodide (PI, 99.5%) were purchased from Macklin Biochemical Technology. Metal electrodes, including Gold (99.999%) and copper (99.999%), were purchased from ZhongNuo Advanced Material (Beijing) Technology. All the super-dry solvents, including methanol, isopropanol (IPA), *N*,*N*-dimethylformamide (DMF), dimethyl sulfoxide (DMSO) and chlorobenzene (CB) used in device fabrication were purchased from J&K Scientific. The FTO (8 Ω sq^{-1}) glasses were purchased from Suzhou ShangYang Solar Technology.

Preparation of perovskite films

1.55-eV perovskite for single-junction PSCs. For the composition of $Cs_{0.05}MA_{0.05}FA_{0.90}PbI_3$, a 1.7-M perovskite precursor solution was prepared by mixing CsI, MAI, FAI and PbI_2 in mixed solvent according to the stoichiometric ratio. An additional 9 mol% PbI_2, 10 mol% MACl and 0.2 mol% GBAC were added to the precursor for crystallization regulation. The perovskite precursor was then stirred for 2 h at room temperature and then filtered through a 0.22-μm filter before use. Then, 50 μl of the filtered precursor solution was spin-coated onto the substrate using a two-step programme: 1,000 rpm for 10 s, followed by 5,000 rpm for 30 s. Then, 200 μl of CB as antisolvent was dripped onto the spinning film 12 s before the end of the second step. Subsequently, the wet film was immediately transferred onto a hotplate and annealed at 100 °C for 30 min.

1.68-eV perovskite for single-junction PSCs. For the composition of $Cs_{0.1}MA_{0.1}FA_{0.8}Pb(I_{0.8}Br_{0.2})_3$, a 1.4-M perovskite precursor solution was prepared by mixing CsI, MAI, FAI, PbI_2 and $PbBr_2$ in mixed solvent according to the stoichiometric ratio. An additional 3 mol% PbI_2 and 0.3 mol% GBAC were added to the precursor for crystallization regulation[41]. The perovskite precursor was then stirred for 2 h at room temperature and then filtered through a 0.22-μm filter before use. Then, 50 μl of the filtered precursor solution was spin-coated onto the substrate using a two-step programme: 1,000 rpm for 2 s, followed by 5,000 rpm for 40 s. Then, 180 μl of CB as antisolvent was dripped onto the spinning film 25 s before the end of the second step. Subsequently, the wet film was immediately transferred onto a hotplate and annealed at 100 °C for 10 min.

1.77-eV perovskite for single-junction PSCs. For the composition of $Cs_{0.1}MA_{0.1}FA_{0.8}Pb(I_{0.6}Br_{0.4})_3$, a 1.2-M perovskite precursor solution was prepared by mixing CsI, MAI, FAI, PbI_2 and $PbBr_2$ in mixed solvent according to the stoichiometric ratio. An additional 5 mol% PbI_2 and 0.3 mol% GBAC were added to the precursor for crystallization regulation. The perovskite precursor was then stirred for 2 h at room temperature and then filtered through a 0.22-μm filter before use. Then, 50 μl of the filtered precursor solution was spin-coated onto the substrate using a two-step programme: 1,000 rpm for 10 s, followed by 5,000 rpm for 40 s. Then, 200 μl of CB as antisolvent was dripped onto the spinning film 20 s before the end of the second step. Subsequently, the wet film was immediately transferred onto a hotplate and annealed at 100 °C for 10 min.

Solar cell fabrication

Pre-patterned FTO glasses were ultrasonically cleaned consecutively with detergent, deionized water and ethanol for 20 min. The FTO glasses substrates were dried with nitrogen flow and treated with ozone–UV light for 15 min before the deposition of HSMs. The HSM solutions (including CbzNaph, CbzNaphBF and CbzNaphBT; 2.0 mM in ethanol/DMF mixed solvents) were spin-coated on FTO glasses at 5,000 rpm for 30 s, followed by annealing at 100 °C for 10 min. For the preparation of HE-MCs, three molecules were mixed in a 1:1:1 molar ratio and maintained the spin-coating parameters. The HE-MCs used for normal-bandgap PSCs were also applicable to wide-bandgap PSCs. The multiple-bandgap perovskite solutions were spin-coated on the HSM-coated substrates according to the aforementioned method. For the surface passivation, PI solution (0.04 mg ml^{-1} dissolved in IPA) was spin-coated onto as-prepared perovskite films at 5,000 rpm for 30 s, followed by annealing at 100 °C for 5 min. The perovskite samples were then transferred into a vacuum chamber and thermally evaporated a 30-nm C_{60} layer under high vacuum ($<6 \times 10^{-6}$ Torr). Subsequently, the samples were loaded into the atomic layer deposition reactor, where a 40-nm-thick SnO_2 film was grown at 100 °C using tetrakis(dimethylamino)tin(IV) (TDMA-Sn) as the tin precursor and water as the oxidant. A 100-nm Cu layer was ultimately thermally evaporated to serve as the top electrode. Note that 120 nm MgF_2 was thermally evaporated on to the backside of completed devices to reduce reflection losses.

Solar cell characterization

The photovoltaic parameters of the devices were evaluated using a Keithley 2400 source meter and an Enlitech SS-F7-3A solar simulator under standard AM1.5G irradiation at 100 mW cm^{-2}. The light intensity was calibrated with a reference monocrystalline silicon cell (Newport 532 ISO1599) traceable to NIST standards. *J*–*V* scan characteristics were recorded via voltage sweeps in both forward and reverse directions, employing scan rates of 0.01 V s^{-1} for single-junction cells, with a fixed measurement delay of 10 ms. Steady-state efficiency was determined by maintaining the bias voltage corresponding to the MPP during continuous illumination. EQE curves were obtained using an EQE measurement system (QE-R, EnliTech).

Other characterizations

^{1}H NMR and ^{13}C NMR spectra were measured on Bruker AVANCE III 400-MHz and 600-MHz spectrometers. Solution UV–visible absorption spectra were obtained from an Agient8454 spectrophotometer, which were collected from the isopropanol solution of two molecules with the concentration of 1.0×10^{-5} M. Cyclic voltammetry measurements were carried out on a CHI660D electrochemical workstation (CH Instruments). Thermal gravity analyses were carried out on a Mettler-Toledo-TGA2 analyser at a heating and cooling rate of 10 K min^{-1}. Cyclic voltammetry measurements were conducted on a CHI660D electrochemical workstation. The contact angle measurements were performed using KRUSS DSA25 standard contact angle measuring instrument. The X-ray diffractometer patterns were performed by using a Rigaku Smartlab equipped with Cu Kα radiation in the 2θ range of 5–45° at a scanning rate of 10° min^{-1}. The TRPL measurements were performed using an Edinburgh Instrument FLS1000 system with a 450-nm laser as the excitation source. XPS and ultraviolet photoelectron spectroscopy measurements were performed using an ultrahigh vacuum surface analysis system equipped with an ULVAC-PHI 5000 VersaProbe III spectrometer with He I ($h\nu$ = 21.22 eV) acting as the excitation source at an energy resolution of 50 meV. GIWAXS measurements were conducted on a Xenocs Xeuss 3.0 UHR system. A high-brilliance monochromatic X-ray beam with an energy of 8.04 keV was directed onto the samples at an incidence angle of 0.5°. For TAS measurements, a commercial TAS system (TA100, TIME TECH SPECTRA) was used on the basis of a second harmonic non-collinear optical parametric amplifier (2HNOPA, Light Conversion) to generate the pump pulses at 650 nm. GIWAXS of thin films were measured at beamline BL14B1 of the Shanghai Synchrotron Radiation Facility using X-rays with an energy of 12.12 keV and an incident angle of 0.5° for the samples. The CCLs are estimated on the basis of the Scherrer equation

(CCL = 2πK/FWHM), where K is the shape factor (here we use K = 0.93), and FWHM is the full-width at half-maximum of the diffraction peaks. The spatial distribution of HSM components was characterized by AFM-IR spectroscopy using the nanoIR2 system (Anasys Instruments).

Stability tests of solar cells

The devices used for stability tests were encapsulated as previously described[42]. The thermal stability for unencapsulated devices was evaluated on a hotplate maintained at a temperature of 85 °C within an N_2-filled glovebox (O_2 <10 ppm, H_2O <0.1 ppm), and the corresponding J–V curves were recorded at different time intervals. The thermal cycling test was conducted with temperature cycling between room temperature and 85 °C in dark, at a ramp rate of 100 °C h^{-1}. The J–V characteristics of devices were conducted after 10, 20, 50, 100, 200, 300, 400, 500, 700 and 1,000 cycles. The long-term operational stability of the devices was characterized using an N_2-filled multi-channels Solar Cell Stability Test System (Wuhan 91PVKSolar Technology) under a white-light LED simulator calibrated to the standard one-sun condition. During the MPP tracking, the device-contained chamber was placed in in ambient air with a relative humidity of 50–60% and was heated to 85 °C by a temperature-control system. Note that the corresponding device was prepared with an architecture of FTO/HE-MCs/perovskite/atomic layer deposition-SnO_2/indium zinc oxide/Cu, where a 50-nm-thick indium zinc oxide layer was sputtered to prevent electrode erosion and the passivation layer was removed.

Computational methodology

MD simulations were performed with the LAMMPS package[43] and the optimized potentials for liquid simulations–all-atom (OPLS-AA) force field[44–47]. The long-range corrected DFT calculations were carried out to re-parameterize the OPLS-AA force field for the CbzNaph, CbzNaphBF and CbzNaphBT molecules. Specifically, their geometries were first optimized at the ωB97XD/6-31G(d,p) level of theory; the bond lengths and angles were then directly taken from the optimized structures while maintaining the original harmonic force constants; and the partial atomic charges were finally fitted by the DFT-calculated electrostatic potentials. Here, the long-range corrected DFT calculations were performed with the Gaussian 16C.01 package.

To model the neat CbzNaph, CbzNaphBF and CbzNaphBT films and the ternary-mixed film, four cubic cells were built with an initial density of 0.2 g cm^{-3}. For the neat film, 200 CbzNaph, CbzNaphBF or CbzNaphBT molecules were randomly placed in the cell; for the mixed film, 100 CbzNaph, 100 CbzNaphBF and 100 CbzNaphBT molecules were placed in the cell. The following MD simulations were run in the *NPT* (constant number of molecules, pressure and temperature) ensemble for 10 ns at a temperature of 500 K and a pressure of 1 atm. Then, the systems were (1) cooled from 500 K to 373.15 K at a rate of 50 K ns^{-1}, (2) kept at 373.15 K for 10 ns, (3) annealed to room temperature in 20 K decrements every 5 ns and (4) kept at room temperature for 10 ns. A cutoff of 12 Å was used for the summation of the van der Waals interactions and the particle–particle particle–mesh solver for the long-range Coulomb interactions. The Verlet integrator was used with a timestep of 1 fs and the Nosé–Hoover thermostat/barostat was employed for temperature/pressure control.

The semi-classical Marcus theory was used to evaluate the intermolecular hole-transfer rate, k_h, for the π–π packing dimers extracted from the MD simulations[48]

$$k_h = \frac{2\pi}{\hbar}\frac{|V_i|^2}{\sqrt{4\pi\lambda_i k_B T}}\exp\left[-\frac{(\Delta E_i + \lambda)^2}{4\lambda_i k_B T}\right],$$

where $\hbar$ represents the reduced Planck's constant, V_i is the electronic coupling between the initial and final states, λ_i is the reorganization energy, k_B is the Boltzmann constant, T is the temperature (298.15 K) and ΔE_i is the energy difference between the initial and final states. V_i or ΔE_i between the initial and final states was approximated as that between the highest occupied molecular orbitals of two molecules in the π–π packing dimer; V_i was evaluated by the fragment orbital method[49]. The λ_i reorganization energy consists of intra- (λ_{intra}) and intermolecular (λ_{inter}) contributions. The former was evaluated from the adiabatic potential energy surfaces of the molecular states involved in the hole-transfer process, while the latter was set to 0.1 eV (a reasonable value for extended π-conjugated systems)[50], considering that there are currently no straightforward models to accurately estimate the λ_{inter} value in solid-state environments. Here, the DFT calculations were performed at the ωB97XD/6-31G(d,p) level of theory.

Reporting summary

Further information on research design is available in the Nature Portfolio Reporting Summary linked to this article.

Data availability

All of the data needed to evaluate the conclusions of the study are present in the Article and its Supplementary Information.

References

41. Wang, D. et al. Self-assembled molecules with hydrogen-bond networks enable efficient all-perovskite tandem solar cells. *Nat. Energy* **11**, 436–448 (2026).
42. Chen, M. et al. Localized 2D/3D heterojunction enhances photovoltage for perovskite-organic tandem solar cells. *Nat. Commun.* **17**, 2093 (2026).
43. Plimpton, S. Fast parallel algorithms for short-range molecular dynamics. *J. Comput. Phys.* **117**, 1–19 (1995).
44. Wang, T., Ravva, M. K. & Brédas, J.-L. Impact of the nature of the side-chains on the polymer-fullerene packing in the mixed regions of bulk heterojunction solar cells. *Adv. Funct. Mater.* **26**, 5913–5921 (2016).
45. Wang, T. & Brédas, J.-L. Organic solar cells based on non-fullerene small-molecule acceptors: impact of substituent position. *Matter* **2**, 119–135 (2020).
46. Jorgensen, W. L. & Tirado-Rives, J. The OPLS (optimized potentials for liquid simulations) potential functions for proteins, energy minimizations for crystals of cyclic peptides and crambin. *J. Am. Chem. Soc.* **110**, 1657–1666 (1988).
47. Jackson, N. E. et al. Conformational order in aggregates of conjugated polymers. *J. Am. Chem. Soc.* **137**, 6254–6262 (2015).
48. Marcus, R. A. Electron transfer reactions in chemistry. Theory and experiment. *Rev. Mod. Phys.* **65**, 599–610 (1993).
49. Coropceanu, V. et al. Charge transport in organic semiconductors. *Chem. Rev.* **107**, 926–952 (2007).
50. D'Avino, G., Muccioli, L., Olivier, Y. & Beljonne, D. Charge separation and recombination at polymer–fullerene heterojunctions: delocalization and hybridization effects. *J. Phys. Chem. Lett.* **7**, 536–540 (2016).

Acknowledgements

We acknowledge the Center of Super-Diamond and Advanced Films of City University of Hong Kong for TAS testing. We also acknowledge E. K. C. Law from the Department of Chemistry at City University of Hong Kong for his assistance with the DOSY measurements.

Author contributions

D.W., W.J. and A.K.-Y.J. conceived the original idea and designed the research. D.W. fabricated all the devices and conducted the major characterizations. W.J. designed and synthesized HSMs with the help of C.-T.W. M.C. contributed to the monitoring of device stability. Q.L. conducted transient absorption spectroscopy. J.F., G.L. and T.W. performed DFT calculations and molecular dynamics simulations

under the supervision of Q.J. D.W. and W.J. wrote the initial manuscript, which was revised by A.K.-Y.J. All authors analysed the data and finalized the manuscript.

Funding

A.K.-Y.J. thanks the sponsorship of the Lee Shau-Kee Chair Professor (Materials Science), and the support from the APRC (grant nos. 9380086, 9610419, 9610440, 9610492 and 9610508) of the City University of Hong Kong; the MHKJFS grant (MHP/054/23), TCFS grant (GHP/121/22SZ) and MRP grant (MRP/040/21X) from the Innovation and Technology Commission of Hong Kong; and the GRF grants (11307621, 11316422, 11308625 and 11308826) and CRS grants (CRS_CityU104/23 and CRS_HKUST203/23) from the Research Grants Council of Hong Kong. This work was partially financially supported by City University of Hong Kong (9610739) for the project 'Fostering Innovation for Resilience and Sustainable Transformation', officially endorsed by the United Nations Educational, Scientific and Cultural Organization under the International Decade of Sciences for Sustainable Development (2024–2033). T.W. is grateful to the National Key R&D Program of China (grant no. 2023YFB3003001) and the National Natural Science Foundation of China (grant no. 52130101) for their support. W. J. is grateful for the support from the Start-up Fund and Young Scientist Cultivation Program (Sun Yat-sen University, 2026QNPY01).

Competing interests

The authors declare no competing interests.

Additional information

Supplementary information The online version contains supplementary material available at https://doi.org/10.1038/s41566-026-02028-5.

Correspondence and requests for materials should be addressed to Tonghui Wang, Wenlin Jiang or Alex K.-Y. Jen.

Peer review information *Nature Photonics* thanks Meng Li, Changduk Yang and the other, anonymous, reviewer(s) for their contribution to the peer review of this work.

Reprints and permissions information is available at www.nature.com/reprints.

nature portfolio

Corresponding author(s): Tonghui Wang, Wenlin Jiang, Alex K.-Y. Jen

Solar Cells Reporting Summary

Nature Portfolio wishes to improve the reproducibility of the work that we publish. This form is intended for publication with all accepted papers reporting the characterization of photovoltaic devices and provides structure for consistency and transparency in reporting. Some list items might not apply to an individual manuscript, but all fields must be completed for clarity.

For further information on Nature Research policies, including our data availability policy, see Authors & Referees.

Experimental design

Please check the following details are reported in the manuscript, and provide a brief description or explanation where applicable.

1. Dimensions

Area of the tested solar cells	☒ Yes	0.068 cm2
	☐ No	*Explain why this information is not reported/not relevant.*
Method used to determine the device area	☒ Yes	The active area was determined by the aperture shade mask placed in front of the device.
	☐ No	*Explain why this information is not reported/not relevant.*

2. Current-voltage characterization

Current density-voltage (J-V) plots in both forward and backward direction	☒ Yes	We performed forward and backward scans on the devices, as illustrated in Fig. 5b and Supplementary Fig. 67.
	☐ No	
Voltage scan conditions	☒ Yes	The J-V curves were obtained from a forward scan (-0.1 V to 1.22 V) and reverse scan (1.22 V to -0.1 V) with a delay time of 10 ms.
	☐ No	*Explain why this information is not reported/not relevant.*
Test environment	☒ Yes	The devices were non-encapsulated and the measurements were conducted in an N2-filled glove box at room temperature.
	☐ No	*Explain why this information is not reported/not relevant.*
Protocol for preconditioning of the device before its characterization	☐ Yes	*Provide a description of the protocol.*
	☒ No	No preconditioning is used before the characterization
Stability of the J-V characteristic	☒ Yes	Reference to third-party certified steady-state efficiency
		Explain why this information is not reported/not relevant.
	☐ No	

3. Hysteresis or any other unusual behaviour

Description of the unusual behaviour observed during the characterization	☐ Yes	*Provide a description of hysteresis or any other unusual behaviour observed during the characterization.*
	☒ No	No unusual behavior was observed during the characterization.
Related experimental data	☒ Yes	We provided J-V hysteresis scans in Fig. 5b and Supplementary Fig. 67.
	☐ No	*Explain why this information is not reported/not relevant.*

4. Efficiency

External quantum efficiency (EQE) or incident photons to current efficiency (IPCE)	☒ Yes	EQE spectra were provided in Supplementary Fig. 61 and 66.
	☐ No	*Explain why this information is not reported/not relevant.*
A comparison between the integrated response under the standard reference spectrum and the response measure under the simulator	☒ Yes	The values of integrated current density from EQE and the short-circuit current density from J-V curve measured under solar simulator are matched well (within 3% difference).
	☐ No	*Explain why this information is not reported/not relevant.*

For tandem solar cells, the bias illumination and bias voltage used for each subcell

☐ Yes
☒ No

Provide a description of the measurement conditions.

No tandem solar cells

5. Calibration

Light source and reference cell or sensor used for the characterization

☒ Yes
☐ No

The devices were measured by Enlitech Solar Simulator SS-F7-3A which offered the simulated AM 1.5G illumination. The monocrystalline silicon cell (Newport 532 ISO1599) was used as a reference cell.

Explain why this information is not reported/not relevant.

Confirmation that the reference cell was calibrated and certified

☒ Yes
☐ No

The reference silicon solar cell was certified by National Institute of Standards and Technology (NIST).

Explain why this information is not reported/not relevant.

Calculation of spectral mismatch between the reference cell and the devices under test

☐ Yes
☒ No

Provide a value of the spectral mismatch and/or a description of how it has been taken into account in the measurements.

No spectral mismatch calculation was performed.

6. Mask/aperture

Size of the mask/aperture used during testing

☒ Yes
☐ No

Aperture masks of 0.068 cm2 were used during testing.

Explain why this information is not reported/not relevant.

Variation of the measured short-circuit current density with the mask/aperture area

☐ Yes
☒ No

Report the difference in the short-circuit current density values measured with the mask and aperture area.

No significant variations were observed.

7. Performance certification

Identity of the independent certification laboratory that confirmed the photovoltaic performance

☒ Yes
☐ No

The tandem cells were sent out for certification in a third-party organization, Tianjin Institute of Metrological Supervision and Testing (TIMST).

Explain why this information is not reported/not relevant.

A copy of any certificate(s)

☒ Yes
☐ No

The copies of certificates were provided in Supplementary Fig. 62.

Explain why this information is not reported/not relevant.

8. Statistics

Number of solar cells tested

☒ Yes
☐ No

The data from 10 cells were statistically analyzed.

Explain why this information is not reported/not relevant.

Statistical analysis of the device performance

☒ Yes
☐ No

The information were provided in Fig. 5a and Supplementary Fig. 58 and 59.

Explain why this information is not reported/not relevant.

9. Long-term stability analysis

Type of analysis, bias conditions and environmental conditions

☒ Yes
☐ No

The operational stabilities of the encapsulated devices was tested, as shown in Fig. 5e. The detailed conditions can be found in Methods section.

Explain why this information is not reported/not relevant.